arXiv:2005.01368v1 [cond-mat.mes-hall] 4 May 2020

Large interfacial spin-orbit torques in layered antiferromagnetic insulator $NiPS_3$/ferromagnet bilayers

C. F. Schippers,[1,*] H. J. M. Swagten,[1] and M. H. D. Guimarães[1,2,†]

[1] *Department of Applied Physics, Eindhoven University of Technology, P.O. Box 513, 5600 MB, Eindhoven, the Netherlands*

[2] *Zernike Institute for Advanced Materials, University of Groningen, P.O. Box 221, 9747 AG, Groningen, the Netherlands*

(Dated: December 22, 2024)

Abstract

Finding efficient ways of manipulating magnetic bits is one of the core goals in spintronic research. Electrically-generated spin-orbit torques (SOTs) are good candidates for this and the search for materials capable of generating highly-efficient SOTs has gained a lot of traction in the recent years. While antiferromagnet/ferromagnet bilayer structures have been employed extensively for passive applications, e.g. by using exchange bias fields, their active properties are not yet widely employed. Here we show the presence of large interfacial SOTs in bilayer of a ferromagnet and the two-dimensional layered antiferromagnetic insulator $NiPS_3$. We observe a large in-plane damping-like interfacial torque, showing a torque conductivity of $\sigma_{\mathrm{DL}} \approx 1 \times 10^5\,(\frac{\hbar}{2\mathrm{e}})/(\Omega\mathrm{m})$ even at room temperature, comparable to the best devices reported in the literature for standard heavy-metal-based and topological insulators-based devices. Additionally, our devices also show an out-of-plane field-like torque arising from the $NiPS_3$/ferromagnet interface, further indicating the presence of an interfacial spin-orbit coupling in our structures. Temperature-dependent measurements reveal an increase of the SOTs with a decreasing temperature below the Néel temperature of $NiPS_3$ ($T_N \approx 170\,\mathrm{K}$), pointing to a possible effect of the magnetic ordering on our measured SOTs. Our findings show the potential of antiferromagnetic insulators and two-dimensional materials for future spintronic applications.

I. INTRODUCTION

The electrical manipulation of magnetization is a promising approach for novel non-volatile and energy efficient memory devices. An especially efficient approach uses current-induced spin-orbit torques (SOTs)[1,2], where an electric current flows through a material with high spin-orbit coupling, which applies a torque on an interfaced magnetic material. These torques can arise from bulk effects, such as the spin-Hall effect,[3,4] where the electrons in a charge current flowing through a conducting layer get deflected to opposite directions depending on their spin. This is the main mechanism for current-induced SOTs in heavy metal/ferromagnet bilayer structures, such as Pt/Permalloy ($Ni_{80}Fe_{20}$; Py)[1]. Interfacial effects, such as the Rashba-Edelstein Effect[5,6], can also generate a sizeable charge-to-spin conversion and can be used for SOT generation[7–9]. More recently, it has been shown that when SOTs are generated in metallic ferromagnetic[10–12] and antiferromagnetic materials[13–15], the magnetic ordering can be used to control the direction and magnitude of the generated SOTs[16]. Even though magnetic insulators have been investigated extensively for the generation of spin currents via spin-pumping[17,18] and spin Seebeck effects[19,20] the use of antiferromagnet insulators in spin-orbit torque devices remains vastly unexplored.

$NiPS_3$ is a layered semiconducting antiferromagnetic van der Waals crystal with a Néel transition temperature of approximately 170 K in its bulk form[21]. Below the transition temperature the magnetic moments of the hexagonally-arranged Ni atoms align in a zigzag fashion, where the coupling is ferromagnetic along a zigzag line and antiferromagnetic across it[22]. Due to its semiconducting nature and relatively flat band dispersion, $NiPS_3$ presents a very high resistivity unless heavily doped or under ultraviolet (UV) light illumination[23,24]. Moreover, $NiPS_3$ also presents promising efficient catalytic properties for hydrogen evolution reaction. Therefore, its main applications so far have been focused on UV light detectors and electro-catalysis[25].

Layered van der Waals materials coupled with 3D ferromagnets have recently been used to explore SOTs, demonstrating promising efficiencies and interesting effects[26–31]. In particular, monolayers of two-dimensional semiconductors have shown large interfacially-generated SOTs[26,27,29,30]. Moreover, it has been shown that layered van der Waals materials possessing low crystal symmetry can give rise to SOTs which are in principle forbidden by symmetry in standard systems, such as Pt/Py[28,29]. However, the microscopic mechanisms behind the

generation of SOTs in van der Waals materials are still poorly understood. It is theoretically predicted that SOTs with interfacial origins can give rise to both field-like (τ_{FL}) and damping-like (τ_{DL}) SOTs[7,8]. These torques usually have forms $\tau_{\mathrm{DL}} \propto \hat{m} \times \hat{y}$ and $\tau_{\mathrm{FL}} \propto \hat{m} \times (\hat{m} \times \hat{y})$, where $\hat{m}$ indicates the magnetization direction and $\hat{y}$ points in the direction perpendicular to the charge current.

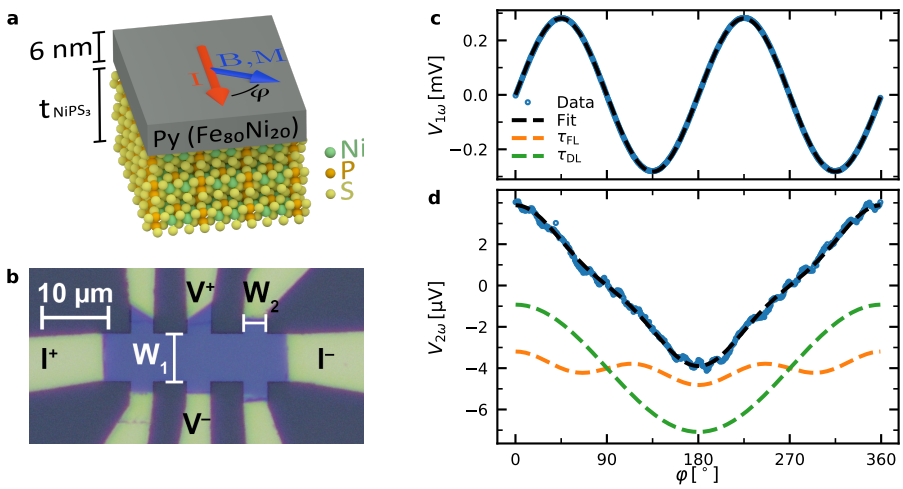

FIG. 1. **Sample geometry and typical measurements.** a) Schematic of the $NiPS_3$/Py bilayers used in the second-harmonic Hall measurements. b) Optical micrograph of a typical Hall bar device used (Device D1). The light blue region in the centre is the Hall bar, patterned from $NiPS_3$/Py/Al(Ox); the golden regions are the Au-covered contact leads. Colours have been enhanced for clarity. First- (c) and second-(d) harmonic Hall voltage as a function in-plane magnetic field angle φ, at room temperature (300 K) and a magnetic field of 34 mT for device D1. The first-harmonic Hall voltage is fitted with Eq. (1) and the second-harmonic with Eq. (2), where the individual contributions of τ_{FL} and τ_{DL} are separately shown, with an arbitrary offset. For both harmonics, a constant background has been removed.

Here we show that a $NiPS_3$/Py bilayer device can also provide large current-induced interfacial SOTs at room temperature, with an in-plane damping-like interfacial torque comparable to the best topological insulators/ferromagnet[32] and heavy-metal (e.g. Pt)/ferromagnet devices[1]. In addition to the in-plane damping-like torque we also observe a weaker out-of-plane field-like torque which also is of interfacial nature. Temperature-dependent measurements across the Néel temperature of $NiPS_3$ show an increasing SOT efficiency, for both in-plane damping-like and out-of-plane field-like torques, indicating a possible influence of

the magnetization ordering of $NiPS_3$ on the SOTs[33]. Our results demonstrate a promising route for the use of (layered) antiferromagnetic insulators for efficient manipulation of magnetic bits.

Our devices are schematically shown in Fig. 1a. The device preparation is described in detail in the Methods section. In short, thin $NiPS_3$ crystals are mechanically exfoliated from a commercially available $NiPS_3$ crystal (HQ Graphene). The exfoliation is performed in vacuum, with pressures $<10^{-6}$ mbar, to maintain a high interface quality of the $NiPS_3$ flakes. Without breaking vacuum, 6 nm of Py is sputter-deposited on the sample followed by a thin 1.5 nm Al capping layer which was naturally oxidized after exposing the samples to atmosphere. The thickness and flatness of the flakes is characterized using atomic force microscopy (AFM). All the selected flakes for device fabrication showed a roughness below 0.5 nm root-mean-square (RMS) in AFM images. In the main text we focus on two devices with different values for $NiPS_3$ layer thickness: device D1, where the $NiPS_3$ flake has a thickness of $t_{NPS} = 3.15$ nm, and device D2, with $t_{NPS} = 6.34$ nm, corresponding to 4 and 9 layers of $NiPS_3$[34], respectively. Measurements for one additional device and for different current-voltage configurations can be found in the Supplementary Materials. The Hall bars were then defined using standard electron-beam lithography and ion-beam milling techniques, followed by another lithography step and electron-beam evaporation to define the Ti(10 nm)/Au(100 nm) leads. Figure 1b shows an optical micrograph of a finished device.

II. RESULTS AND DISCUSSION

The harmonic Hall measurements were performed using standard low-frequency (17 Hz) lock-in techniques. A current $I_0 \approx 2.5$ mA was driven between the outer contacts and the induced Hall voltage, in the first ($V_{\mathrm{H}}^{1\omega}$) and second ($V_{\mathrm{H}}^{2\omega}$) harmonic of the frequency used, was detected between the arms of the Hall bar. Simultaneously, a magnetic field $\boldsymbol{B}$ was applied in the sample plane under an angle φ with respect to the current direction (Fig. 1a). Assuming the magnetization $\boldsymbol{M}$ of the Py layer aligns to the external magnetic field, $V_{\mathrm{H}}^{1\omega}$ is given by:

$$V_{\mathrm{H}}^{1\omega} = I_0 R_{\mathrm{P}} \sin 2\varphi \cos^2 \vartheta + I_0 R_{\mathrm{A}} \cos \vartheta, \tag{1}$$

where ϑ is the polar angle of the magnetic field (i.e. the angle with respect to the sample normal), R_{P} is the planar Hall resistance and R_{A} is the anomalous Hall resistance.

The first harmonic Hall voltage as a function of φ for a fixed value of $B = 34\,\mathrm{mT}$ at room temperature (300 K) for device D1 is shown in Fig. 1c as an example of a typical measurement (other measurements on both the same device and other devices have similar signal-to-noise ratios and curve fitting quality). The measurement is corrected for a small phase offset caused by a small misalignment of the current direction with the x-axis of our experimental set-up. We observe a $\sin(2\varphi)$-behaviour with the values for R_P in our devices obtained by fitting our measurement using Eq. (1). Similarly, we extract the value for R_A through out-of-plane magnetic field measurements, as detailed in the Supplementary Information. The values R_P and R_A are used to quantify the measured spin-torque values that we discuss later in the text.

Bulk $NiPS_3$ belongs to the symmetry group $C2/m$ in its paramagnetic state[22,34–36], presenting one rotation axis, a glide mirror plane, and an inversion point. Below the Néel transition temperature, the magnetic texture further reduces the symmetries of the bulk to a single mirror plane, space group Pm[22]. Therefore, one could expect an induced magnetic anisotropy as reported for the low-symmetry layered materials (e.g. WTe_2 and $TaTe_2$)[28,29,31]. Moreover, the antiferromagnetic ordering of $NiPS_3$ could also induce an exchange bias on the Py if the magnetic structure is not strictly collinear or a small exchange bias via a perpendicular coupling at the interface of the antiferromagnetic spins of $NiPS_3$ and the ferromagnetic spins of Py[37]. In the measurement shown in Fig. 1c we do not find a significant deviation from the fit with Eq. (1), which does not take into account any anisotropy or exchange bias. Hence, we do not observe an induced magnetic anisotropy or exchange bias induced by our $NiPS_3$ crystals (see Supplementary Information for further measurements). The lack of an induced in-plane magnetic anisotropy is in agreement with measurements in devices based on high-symmetry transition metal dichalcogenide (TMD) crystals[26,27,30]. This indicates that the magnetic anisotropy as observed in the low-symmetry materials is most likely strongly dependent on the specifics of the electronic properties and exchange coupling of the bilayer structure. Moreover, the lack of an observable exchange bias upon field-cooling the device through the Néel temperature agrees with the expected collinear magnetic ordering in our $NiPS_3$ crystals.

In addition to a first harmonic response, the presence of a non-negligible current-induced SOT gives rise to a Hall voltage in the second harmonic of the current[38,39]. Assuming that the magnetization direction follows the applied magnetic field, the second harmonic Hall

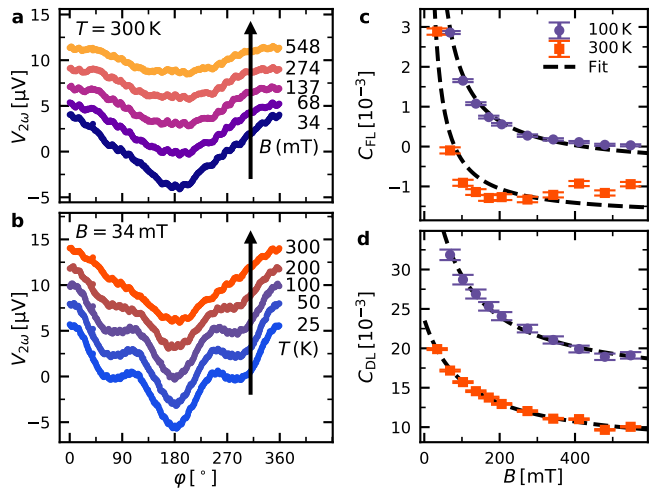

FIG. 2. **Field and temperature dependence of the second-harmonic Hall voltage.** The second-harmonic Hall voltage $V_{2\omega}$ is measured as a function of in-plane field angle φ for a number of magnetic field strengths B (a) and temperatures (b). For clarity an arbitrary offset has been added to the measurements. c) and d) show the magnetic field dependence of coefficients C_{FL} and C_{DL} for different temperatures.The fits are performed as described in the text.

voltage, $V_{\mathrm{H}}^{2\omega}$, is given by[29]:

$$V_{\mathrm{H}}^{2\omega} = -I_0 R_{\mathrm{P}} C_{\mathrm{FL}} \cos 2\varphi \sin\varphi - \frac{1}{2} I_0 R_{\mathrm{A}} C_{\mathrm{DL}} \sin\varphi, \tag{2}$$

where C_{FL} and C_{DL} are coefficients proportional to the out-of-plane field-like and in-plane damping-like torques and given by $C_{\mathrm{FL}} = \frac{\tau_{\mathrm{FL}}}{\gamma B}$, and $C_{\mathrm{DL}} = \frac{\tau_{\mathrm{DL}}}{\gamma(B+B_{\mathrm{K}})} + \frac{2V_{\mathrm{ANE}}}{I_0 R_{\mathrm{A}}}$. Here γ is the gyromagnetic ratio and B_{K} the total effective anisotropy field, including the demagnetization and perpendicular magnetic anisotropy, and V_{ANE} is the anomalous Nernst contribution.

Figure 1d shows a typical measurement of the second harmonic Hall voltage as a function of the in-plane magnetic field angle φ. The contributions by the different torques τ_{FL} and τ_{DL} can be obtained by fitting our data using the equation above, and their individual contributions to the fit are shown in Fig. 1d. To disentangle other unwanted contributions on our signals, such as the anomalous Nernst effect[27] we perform angular dependence measurements for various values of applied magnetic field[40,41].

Figure 2 shows second harmonic Hall measurements for various values of the external magnetic field strength and temperatures. Here we see that the line shape of the second harmonic Hall measurement changes with both the external magnetic field for a fixed tem-

perature (Fig. 2a), and as a function of temperature for a fixed magnetic field (Fig. 2b), indicating a change in weight for the different contributions for τ_{DL} and τ_{FL} in our devices. We fit the angle-dependent measurements for different fields and temperatures using Eq. (2). There we include a constant offset to account for terms unrelated to current-induced spin-orbit torque such as thermal effects (anomalous Nernst effect)[27], and use R_{A} and R_{P} as determined earlier. Values for the coefficients C_{FL} and C_{DL} are obtained for each individual measurement, shown in Fig. 2c and d. The current-induced SOTs are then quantified by fitting C_{FL} and C_{DL}, as described earlier, shown as dashed lines in Fig. 2c and d, to extract τ_{FL} and τ_{DL}. It has been reported that spin-orbit torque measurements using the second harmonic Hall technique can be influenced by the aspect ratio of the Hall bar dimensions (W_2/W_1 as specified in Fig. 1a)[42]. Therefore, in order to better quantify our results, the values for the torques (i.e. τ_{FL} and τ_{DL}) we obtained were corrected for our specific Hall bar geometry by dividing the torque value by a factor corresponding to the Hall bar geometry[43].

At room temperature (300 K) we observe an in-plane damping-like $[\hat{m} \times (\hat{m} \times \hat{y})]$ torque $\tau_{\mathrm{DL}}/(\gamma I_0) = (1.0 \pm 0.1)\,\mathrm{mT/mA}$, for device D1. For a better comparison with other devices in literature, the torque value can be evaluated as torque conductivity σ, defined as the angular momentum absorbed by the magnet per second per unit interface area per unit electric field. For a torque τ_i (i= DL or FL), we calculate the corresponding spin-torque conductivity by $\sigma = M_{\mathrm{S}} t_{\mathrm{FM}} \frac{W_1}{R_{\mathrm{S}}} \frac{\tau_i}{\gamma I_0}$, where M_{S} is the saturation magnetization of the Py FM layer, $t_{\mathrm{FM}} = 6\,\mathrm{nm}$ is the thickness of the Py layer, W_1 is the Hall bar width as defined in Fig. 1a, and R_{S} is the sheet resistance of the measured device. We obtain $\sigma_{\mathrm{DL}} = (0.64 \pm 0.09) \times 10^5$ to $(2.2 \pm 0.3) \times 10^5\,(\frac{\hbar}{2\mathrm{e}})/(\Omega\mathrm{m})$ for the in-plane damping-like torque τ_{DL}, using $\mu_0 M_{\mathrm{S}}$ in the range of 0.2 to 0.7 T, respectively[28–31]. This is the largest damping-like torque conductivity for all layered material/ferromagnet devices reported so far, which are over one order of magnitude lower[26–31,44], and is in the range of the best values obtained using standard heavy-metal/ferromagnet devices and topological insulator/ferromagnet devices, in the order of $1 \times 10^5\,(\frac{\hbar}{2\mathrm{e}})/(\Omega\mathrm{m})$[32,40,45].

We also find a non-negligible out-of-plane field-like torque $(\hat{m} \times \hat{y})$ in our $NiPS_3$/Py devices, $\tau_{\mathrm{FL}}/(\gamma I_0) = (0.079 \pm 0.009)\,\mathrm{mT/mA}$ at room temperature, corresponding to a spin-torque conductivity of $(0.49 \pm 0.06) \times 10^4$ to $(1.7 \pm 0.2) \times 10^4\,(\frac{\hbar}{2\mathrm{e}})/(\Omega\mathrm{m})$ (using $\mu_0 M_{\mathrm{S}}$ in the range of 0.2 to 0.7 T). The presence of both damping-like and field-like torques arising from interfacial SOTs are in agreement with theoretical predictions[7,8]. However, the magnitude

for τ_{FL} is about one order of magnitude smaller than the damping-like torques discussed above.

To understand where the observed torque originates from it is instructive to consider the possible current paths through the $NiPS_3$/Py bilayer. Intrinsic $NiPS_3$ is highly resistive[23,24], in sharp contrast to the metallic Py layer, which has a resistivity that is orders of magnitude lower than $NiPS_3$ (of the order of $10^{-5}\,\Omega\,\mathrm{cm}$ for Py compared to $10^{11}\,\Omega\,\mathrm{cm}$ for $NiPS_3$). Hence, we expect that all current flows through the Py layer in our $NiPS_3$/Py devices. This is confirmed by measurements of the sheet resistances R_{S} for $NiPS_3$/Py based devices (140 to $150\,\Omega/\square$) and a Py based device ($\sim 110\,\Omega/\square$), i.e. without a SOT material layer. The small difference in sheet resistance could be attributed to a difference in quality of the Py layer when grown on top of the different surfaces, the $NiPS_3$ flake or the bare Si/SiO_2 substrate. Hence, the torques measured have to arise from the interface between Py and $NiPS_3$; the large values for τ_{DL} observed in our devices indicate the presence of a very strong interfacial SOT.

Other possible contributions to the observed SOTs can arise from the Al capping layer. If the Al capping layer is not completely oxidized, a current path through the Al capping layer allows the generation of an Oersted field working on the Py layer. Alternatively, when a current flows through the Py layer in an inhomogeneous manner, the Oersted field generated by the current through the Py layer do not fully cancel and a net out-of-plane field-like torque can be measured. In order to probe such possible contributions on our results we perform control measurements in devices based on a single Py layer, without a SOT material, but still capped with the naturally-oxidized Al(1.5 nm) layer. For these samples we obtained $\tau_{\mathrm{DL}}/(\gamma I_0) = (-0.018 \pm 0.002)\,\mathrm{mT/mA}$, considerably smaller (and of opposite sign) than the values obtained in our $NiPS_3$ devices. Interestingly, we also observe a measurable, albeit smaller, τ_{FL} for Hall bars based on only Py [$\tau_{\mathrm{FL}}/(\gamma I_0) = (0.0203 \pm 0.0002)\,\mathrm{mT/mA}$], i.e. without a spin-orbit torque generating material. This unexpected torque could be an indication an additional contribution from either an unoxidised portion of the Al capping layer or an inhomogeneous current distribution in the ferromagnetic layer. However, as the SOTs observed in this device are significantly smaller than the SOTs observed in the $NiPS_3$ devices, this shows that the Al oxide capping layer has a minimal effect in our measured torque values and points to the crucial role of the $NiPS_3$ flake on the measured spin-orbit torques in those devices.

We also perform a direct comparison to standard heavy-metal/ferromagnet SOT devices by performing control measurements in a Pt/Py device fabricated using the same procedure as the $NiPS_3$ devices. For these devices we obtain $\tau_{\mathrm{DL}}/(\gamma I_0) = (0.22 \pm 0.01)\,\mathrm{mT/mA}$. This translates to a torque conductivity ranging from $\sigma_{\mathrm{DL}} = (2.2 \pm 0.2) \times 10^5$ to $(7.4 \pm 0.4) \times 10^5\,(\frac{\hbar}{2\mathrm{e}})/(\Omega\mathrm{m})$ (for $\mu_0 M_{\mathrm{S}}$ of 0.2 to 0.7 T), which is in line with the typical torques observed in literature[32,40,45]. This torque is only slightly larger than the torque found in the $NiPS_3$ based device, illustrating that the torque found in the $NiPS_3$ based device is indeed in the range of the best heavy-metal based or topological insulator based devices. Finally, for our Pt/Py devices we observe a $\tau_{\mathrm{FL}}/(\gamma I_0) = (0.231 \pm 0.001)\,\mathrm{mT/mA}$, with a magnitude consistent with the expected Oersted-field contribution from the current flowing in the Pt layer.

Even though a significant out-of-plane field-like torque is observed in all our devices, there is a clear difference between the results in our control Py and Pt/Py devices and the ones for the $NiPS_3$/Py devices: while Py and Pt/Py devices consistently show a positive sign for τ_{FL}, we observe both a positive and negative signs for our $NiPS_3$/Py devices (see Supplementary Information for more measurements). The presence of an interfacial out-of-plane field-like torque has been observed in devices based on TMD monolayers[27], with a sign change with respect to Oersted-fields observed in monolayer $NbSe_2$/Py bilayers[30]. Albeit we cannot completely rule out the possibility of alternative mechanisms for the observed τ_{FL}, such as an inhomogeneous current distribution in the Py layer, the comparison of the results for the three different devices (Py, Pt/Py, and $NiPS_3$/Py) indicate the presence of a non-negligible interfacial out-of-plane field-like torque.

In order to explore the effect of the antiferromagnetic phase transition of $NiPS_3$ on the current-induced SOTs we performed measurements as a function of temperature across $T_{\mathrm{N}} \sim 170\,\mathrm{K}$, with T ranging from 10 K to 300 K. Our devices show a decrease in sheet resistance of about 5% with a decrease in temperature indicating a metallic behaviour (Fig. 3a for device D1), in agreement with the expectation that the resistance in our devices is dominated by the metallic Py layer.

By performing the same procedure for quantifying τ_{DL} and τ_{FL} described above, we extract the temperature dependence of the spin-orbit torques (Fig. 3b and c for τ_{DL} and τ_{FL} respectively). We observe that there is indeed a temperature dependence of both the out-of-plane field-like and in-plane damping-like torque; in device D1 the torques increase

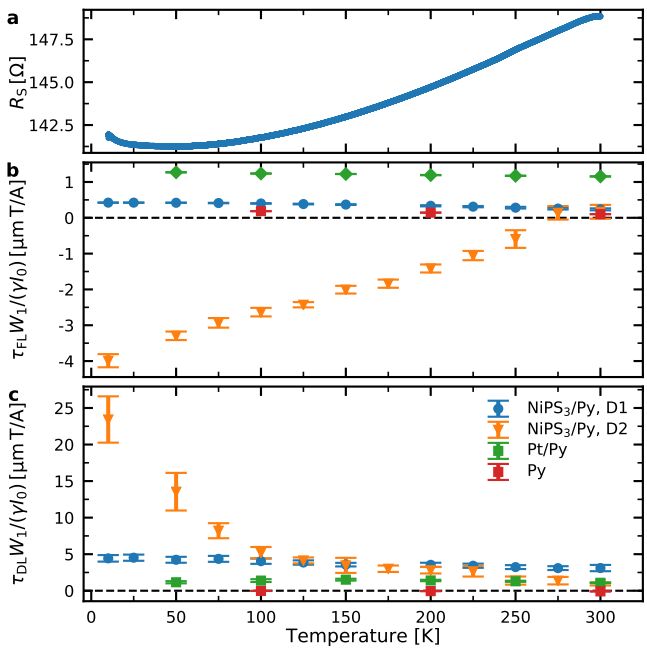

FIG. 3. **Torques as a function of temperature.** a) Sheet resistance R_S of the $NiPS_3$/Py/Al(Ox) Hall bar as a function of temperature. Out-of-plane field-like torque τ_{FL} (b) and in-plane damping-like torque τ_{DL} (c) as a function of temperature in the $NiPS_3$/Py bilayer devices, a Py reference sample, and a Pt/Py reference sample. The measured torques have been corrected for influence of the Hall bar geometry, according to[42], and normalized by the two-dimensional current density (W_1/I_0) for better comparison among devices.

up to (0.141 ± 0.002) mT/mA and (1.4 ± 0.1) mT/mA when lowering the temperature to 10 K for the out-of-plane field-like and in-plane damping-like torques, respectively. For the in-plane damping-like torque this behaviour is consistent over different devices: the torque value increases when the temperature decreases, though the amount of increase is not constant over the different devices (see Supplementary Information). We find no consistent behaviour for the out-of-plane field-like torque in our $NiPS_3$/Py devices apart from the fact that the torque magnitude and sign seem to be strongly dependent on temperature (see Supplementary Information).

The increase for the in-plane damping-like torque with a decrease in temperature seems reproducible among our $NiPS_3$/Py devices, however, we find that the specific trend with temperature is device specific. For device D2 for example, we observe a smaller in-plane damping-like torque at room temperature ($\tau_{DL} = (0.30 \pm 0.06)$ mT/mA) and a much steeper

increase to $(8 \pm 1)\,\mathrm{mT/mA}$ at 10 K, significantly larger than the maximum value in device D1. Interestingly, for all our devices we see an onset on the change in torque magnitude at temperatures near the Néel temperature of $NiPS_3$, around 150 K. Even though this is a qualitative observation, we believe that this is an indication that the magnetic ordering in $NiPS_3$ has an effect on the measured SOTs.

The behaviour of the out-of-plane field-like torque τ_{FL} is different for different devices. For some devices we observe a negative value for τ_{FL} that also increases in magnitude when the temperature is decreased while others show an initially positive torque that changes sign when the temperature is decreased. The reason for these different temperature dependencies (for both the in-plane damping-like and out-of-plane field-like torque) remains unclear and requires further studies. Possible explanations might be related to the thickness of the $NiPS_3$ flake – device D1 contains a relatively thin flake of only 4 layers of $NiPS_3$ while device D2 contains a flake of 9 layers – or to the quality of the interface between the $NiPS_3$ flake and the Py layer, which could e.g. result in a temperature-dependent spin-mixing conductance. Although devices with 3 different $NiPS_3$ thicknesses were measured and both similarities and differences were found, we did not observe a systematic behaviour with thickness. A more systematic study on the thickness dependence is required and is left for future investigations.

We now compare the temperature dependence of the SOTs obtained for our $NiPS_3$/Py to our control Pt/Py and Py devices. Since these devices have slightly different dimensions, we find it better to normalize the torques by the two-dimensional current density (W_1/I_0), Fig. 3b and c. For the Py based device we observe a very small change in both τ_{FL} and τ_{DL}, with values close to zero throughout the whole measured temperature range. For the Pt/Py device we find a small monotonic increase of τ_{FL} with a decrease in temperature, probably indicating that the Pt layer decreases its resistivity faster than the Py layer, therefore increasing the Oersted-field torque in this device. We also observe a small change in τ_{DL} with a change in temperature, but different from the monotonic increase observed for our $NiPS_3$/Py devices. This strengthens the conclusion that both the SOTs observed in the $NiPS_3$/Py devices and their temperature dependence originate from the $NiPS_3$/Py interface.

While the exact origin of the observed spin-orbit torque in the $NiPS_3$/Py devices is not understood at this moment, we suggest two possible mechanisms. First, the inversion symmetry breaking at the $NiPS_3$/Py interface can allow for the presence of a Rashba spin-orbit coupling. This effect has been shown to give rise to strong SOTs in metallic[2],

topological-insulators[2,32] and TMD-based devices[28,29]. Alternatively, a non-collinearity of the antiferromagnetic order in $NiPS_3$ or the ferromagnetic ordering in Py could allow for an effective SOTs to generated even in the absence of a spin-orbit interaction in the $NiPS_3$[33]. Though both $NiPS_3$ and Py present fully collinear magnetic structures, their mutual exchange interaction can lead to a spatially-varying magnetic ordering, thereby adding a small non-collinear contribution to the magnetic order. However, a more in-depth understanding of the nature of the mechanisms involved in generating the observed SOTs requires a more thorough theoretical treatment.

Below the Néel temperature, $NiPS_3$ presents an antiferromagnetic ordering (with ferromagnetic zigzag lines that couple antiferromagnetically)[22] which breaks the glide mirror plane and the screw symmetry axis. It has been shown that a crystallographic (or magnetic) symmetry breaking can lead to non-standard spin-orbit torques[14,28,29,31,33,44]. In order to explore a possible effect of the crystal and magnetic symmetries and orientation on the measured SOTs, we perform the fitting procedure with extra terms representing an out-of-plane damping-like torque ($\hat{m} \times \hat{m} \times \hat{z}$). Additionally, we performed the same measurements and analysis with the current and voltage paths interchanged, i.e. rotated by $\pi/2$. Here the angle between the current and the zigzag line of the magnetic ordering should change for the two configurations which could have an influence on the torques that are generated by the $NiPS_3$/Py interface. We observe only a small difference of a factor of approximately 1.5 in τ_{DL} and smaller for τ_{FL} (see Supplementary Information). As this is reproduced in our control devices it likely arises from the different current paths for the two configurations and seems to be unrelated to the crystal properties of $NiPS_3$. Therefore, no torque components related to the crystal and magnetic symmetries and orientation are observed within our experimental accuracy.

III. CONCLUSION

In conclusion, we observe large interfacial in-plane damping-like SOTs in $NiPS_3$/Py bilayers. Our devices present in-plane damping-like SOTs in the order of (1.0 ± 0.1) mT/mA, compared to (0.22 ± 0.01) mT/mA found a heavy-metal/ferromagnet device (Pt/Py). Additionally, we observe a small interfacial out-of-plane field-like SOT of (0.079 ± 0.009) mT/mA with a direction that is opposite to a torque from Oersted-fields coming from a current

through the $NiPS_3$ flake, which is in line with the high resistivity of $NiPS_3$ that prevents a current from running through the flake. Though we observed a (non-trivial) temperature dependence of the observed SOTs, we found no clear relation to the antiferromagnetic phase-transition of $NiPS_3$ or the related reduction of the crystallographic symmetry. Based on these findings, we conclude that there is a significant contribution of the interface between $NiPS_3$ and Py to both the out-of-plane field-like and in-plane damping-like SOTs, although the microscopic origin is not yet understood.

Our results add to the understanding that the detailed electronic structure of the interface between the spin-orbit material and ferromagnet plays a critical role on the measured SOTs, and should encourage the development of a more complete theoretical framework for the prediction of SOTs using various materials. The large interfacial torque and lack of dependence on the specific crystal symmetries or orientation is ideal for highly-efficient SOT devices. The fact that current flows only through the ferromagnetic layer allows for the use of lower total currents for magnetization switching when compared to standard heavy-metal/ferromagnet devices. Therefore, we believe our results illustrate the potential of insulating van der Waals crystals for spintronic applications.

IV. ACKNOWLEDGEMENTS

We acknowledge B. Koopmans and M. Titov for fruitful discussions and for useful comments on the manuscript, and J. Francke and G. Basselmans for technical help with the experimental setup. Sample fabrication was performed using NanoLabNL facilities. The research performed here was funded by the Dutch Research Council (NWO) under the grants VENI 15093 and 680-91-113.

V. METHODS

A. Sample fabrication

$NiPS_3$ flakes were mechanically exfoliated from commercially available crystals (HQ Graphene) onto a thermally oxidized Si/SiO_2 substrate (with 100 nm SiO_2). For this exfoliation ordinary scotch tape was used. To prevent degradation of the flakes and conserve the high-quality interface of the exfoliated flakes the exfoliation is performed in two steps. First

the tape with flakes is prepared and placed on the substrate in a nitrogen-filled glove-box. The substrate, with tape, is transported (through air) to the load-lock of the deposition system. Here, the actual exfoliation is performed when the load-lock has reached a pressure $<10^{-6}$ mbar.

The sample is then immediately transported, through vacuum, into the deposition chamber, where Py(6)/ Al(1.5) is deposited on the sample by magnetron sputtering. Afterwards, the sample is taken out of the vacuum into air, where the Al layer will oxidise to Al_2O_3, creating an insulating and protective layer for the sample. Using an optical microscope the sample is inspected to find sufficiently large (i.e. larger than 5 µm × 5 µm) $NiPS_3$ flakes for later sample fabrication.

For each sufficiently large flake a Hall bar is designed and patterned into a SiO_2 hard-mask using electron-beam lithography (EBL) with poly-(methyl-methacrylate) (PMMA), sputter deposition of SiO_2 (60 nm), and a lift-off process. The Hall bar is then etched into the $NiPS_3$ flake using argon (Ar) ion-beam milling, a layer of SiO_2 (20 nm) is sputter deposited to clamp the Hall bars on the sample.

Hereafter the Hall bars contacts are fabricated. The contacts are patterned into a layer of PMMA, again using EBL. Using reactive ion etching the SiO_2 layer is removed in places where the contacts will be deposited. Finally, Ti/Au is deposited for the contacts, after a short argon etching to remove the Al_2O_3 on top of the Py for better contacts, and lift-off is performed to remove the PMMA and the redundant Ti/Au.

VI. AUTHOR CONTRIBUTIONS

CFS and MHDG conceived the experiment, fabricated the samples, and performed the measurements while advised by HJMS. CFS performed the data analysis under MHDG and HJMS supervision. CFS and MHDG wrote the manuscript with comments from HJMS.

---

* c.f.schippers@tue.nl

† m.h.guimaraes@rug.nl

[1] L. Liu, T. Moriyama, D. C. Ralph, and R. A. Buhrman, Spin-Torque Ferromagnetic Resonance Induced by the Spin Hall Effect, Physical Review Letters **106**, 036601 (2011).

[2] A. Manchon, H. C. Koo, J. Nitta, S. M. Frolov, and R. A. Duine, New perspectives for Rashba spin-orbit coupling, Nature Materials **14**, 871 (2015).

[3] P. P. Haazen, E. Murè, J. H. Franken, R. Lavrijsen, H. J. Swagten, and B. Koopmans, Domain wall depinning governed by the spin Hall effect, Nature Materials **12**, 299 (2013).

[4] A. van den Brink, G. Vermijs, A. Solignac, J. Koo, J. T. Kohlhepp, H. J. M. Swagten, and B. Koopmans, Field-free magnetization reversal by spin-Hall effect and exchange bias, Nature Communications **7**, 10854 (2016).

[5] V. M. Edelstein, Spin polarization of conduction electrons induced by electric current in two-dimensional asymmetric electron systems, Solid State Communications **73**, 233 (1990).

[6] A. Chernyshov, M. Overby, X. Liu, J. K. Furdyna, Y. Lyanda-Geller, and L. P. Rokhinson, Evidence for reversible control of magnetization in a ferromagnetic material by means of spin-orbit magnetic field, Nature Physics **5**, 656 (2009).

[7] V. P. Amin and M. D. Stiles, Spin transport at interfaces with spin-orbit coupling: Formalism, Physical Review B **94**, 104419 (2016).

[8] V. P. Amin and M. D. Stiles, Spin transport at interfaces with spin-orbit coupling: Phenomenology, Physical Review B **94**, 104420 (2016).

[9] F. Hellman, A. Hoffmann, Y. Tserkovnyak, G. S. Beach, E. E. Fullerton, C. Leighton, A. H. Macdonald, D. C. Ralph, D. A. Arena, H. A. Dürr, P. Fischer, J. Grollier, J. P. Heremans, T. Jungwirth, A. V. Kimel, B. Koopmans, I. N. Krivorotov, S. J. May, A. K. Petford-Long, J. M. Rondinelli, N. Samarth, I. K. Schuller, A. N. Slavin, M. D. Stiles, O. Tchernyshyov, A. Thiaville, and B. L. Zink, Interface-induced phenomena in magnetism, Reviews of Modern Physics **89**, 10.1103/RevModPhys.89.025006 (2017).

[10] K. S. Das, J. Liu, B. J. Van Wees, and I. J. Vera-Marun, Efficient Injection and Detection of Out-of-Plane Spins via the Anomalous Spin Hall Effect in Permalloy Nanowires, Nano Letters **18**, 5633 (2018).

[11] J. D. Gibbons, D. Macneill, R. A. Buhrman, and D. C. Ralph, Reorientable Spin Direction for Spin Current Produced by the Anomalous Hall Effect, Physical Review Applied **9**, 064033 (2018).

[12] C. Safranski, E. A. Montoya, and I. N. Krivorotov, Spin–orbit torque driven by a planar Hall current, Nature Nanotechnology **14**, 27 (2019).

[13] J. Zhou, X. Wang, Y. Liu, J. Yu, H. Fu, L. Liu, S. Chen, J. Deng, W. Lin, X. Shu, H. Y. Yoong, T. Hong, M. Matsuda, P. Yang, S. Adams, B. Yan, X. Han, and J. Chen, Large spin-orbit torque efficiency enhanced by magnetic structure of collinear antiferromagnet IrMn, Science Advances **5**, eaau6696 (2019).

[14] W. Zhang, W. Han, S. H. Yang, Y. Sun, Y. Zhang, B. Yan, and S. S. Parkin, Giant facet-dependent spin-orbit torque and spin Hall conductivity in the triangular antiferromagnet IrMn3, Science Advances **2**, e1600759 (2016).

[15] V. Tshitoyan, C. Ciccarelli, A. P. Mihai, M. Ali, A. C. Irvine, T. A. Moore, T. Jungwirth, and A. J. Ferguson, Electrical manipulation of ferromagnetic NiFe by antiferromagnetic IrMn, Physical Review B **92**, 214406 (2015).

[16] A. Davidson, V. P. Amin, W. S. Aljuaid, P. M. Haney, and X. Fan, Perspectives of electrically generated spin currents in ferromagnetic materials, Physics Letters A **384**, 126228 (2020).

[17] E. Saitoh, M. Ueda, H. Miyajima, and G. Tatara, Conversion of spin current into charge current at room temperature: Inverse spin-Hall effect, Applied Physics Letters **88**, 182509 (2006).

[18] B. Heinrich, C. Burrowes, E. Montoya, B. Kardasz, E. Girt, Y. Y. Song, Y. Sun, and M. Wu, Spin pumping at the magnetic insulator (YIG)/normal metal (Au) interfaces, Physical Review Letters **107**, 066604 (2011).

[19] K. Uchida, J. Xiao, H. Adachi, J. Ohe, S. Takahashi, J. Ieda, T. Ota, Y. Kajiwara, H. Umezawa, H. Kawai, G. E. Bauer, S. Maekawa, and E. Saitoh, Spin Seebeck insulator, Nature Materials **9**, 894 (2010).

[20] G. E. Bauer, E. Saitoh, and B. J. Van Wees, Spin caloritronics, Nature Materials **11**, 391 (2012).

[21] B. L. Chittari, Y. Park, D. Lee, M. Han, A. H. Macdonald, E. Hwang, and J. Jung, Electronic and magnetic properties of single-layer M PX3 metal phosphorous trichalcogenides, Physical Review B **94**, 184428 (2016).

[22] A. R. Wildes, V. Simonet, E. Ressouche, G. J. McIntyre, M. Avdeev, E. Suard, S. A. Kimber, D. Lançon, G. Pepe, B. Moubaraki, and T. J. Hicks, Magnetic structure of the quasi-two-dimensional antiferromagnet NiPS3, Physical Review B **92**, 224408 (2015).

[23] P. Foot, J. Suradi, and P. Lee, Optical and electronic properties of the layered semiconductors NiPS3 and FePS3, Materials Research Bulletin **15**, 189 (1980).

[24] J. Chu, F. Wang, L. Yin, L. Lei, C. Yan, F. Wang, Y. Wen, Z. Wang, C. Jiang, L. Feng, J. Xiong, Y. Li, and J. He, High-Performance Ultraviolet Photodetector Based on a Few-Layered 2D NiPS3

Nanosheet, Advanced Functional Materials **27**, 1701342 (2017).

[25] C. C. Mayorga-Martinez, Z. Sofer, D. Sedmidubský, Š. Huber, A. Y. S. Eng, and M. Pumera, Layered Metal Thiophosphite Materials: Magnetic, Electrochemical, and Electronic Properties, ACS Applied Materials and Interfaces **9**, 12563 (2017).

[26] W. Zhang, J. Sklenar, B. Hsu, W. Jiang, M. B. Jungfleisch, J. Xiao, F. Y. Fradin, Y. Liu, J. E. Pearson, J. B. Ketterson, Z. Yang, and A. Hoffmann, Research Update: Spin transfer torques in permalloy on monolayer MoS2, APL Materials **4**, 10.1063/1.4943076 (2016).

[27] Q. Shao, G. Yu, Y.-W. Lan, Y. Shi, M.-Y. Li, C. Zheng, X. Zhu, L.-J. Li, P. K. Amiri, and K. L. Wang, Strong Rashba-Edelstein Effect-Induced Spin–Orbit Torques in Monolayer Transition Metal Dichalcogenide/Ferromagnet Bilayers, Nano Letters **16**, 7514 (2016).

[28] D. MacNeill, G. M. Stiehl, M. H. Guimarães, R. A. Buhrman, J. Park, and D. C. Ralph, Control of spin-orbit torques through crystal symmetry in WTe2/ferromagnet bilayers, Nature Physics **13**, 300 (2017).

[29] D. MacNeill, G. M. Stiehl, M. H. Guimarães, N. D. Reynolds, R. A. Buhrman, and D. C. Ralph, Thickness dependence of spin-orbit torques generated by WTe2, Physical Review B **96**, 054450 (2017).

[30] M. H. D. Guimarães, G. M. Stiehl, D. MacNeill, N. D. Reynolds, and D. C. Ralph, Spin–Orbit Torques in NbSe 2 /Permalloy Bilayers, Nano Letters **18**, 1311 (2018).

[31] G. M. Stiehl, D. MacNeill, N. Sivadas, I. El Baggari, M. H. D. Guimarães, N. D. Reynolds, L. F. Kourkoutis, C. J. Fennie, R. A. Buhrman, and D. C. Ralph, Current-Induced Torques with Dresselhaus Symmetry Due to Resistance Anisotropy in 2D Materials, ACS Nano , acsnano.8b09663 (2019).

[32] A. R. Mellnik, J. S. Lee, A. Richardella, J. L. Grab, P. J. Mintun, M. H. Fischer, A. Vaezi, A. Manchon, E. A. Kim, N. Samarth, and D. C. Ralph, Spin-transfer torque generated by a topological insulator, Nature **511**, 449 (2014).

[33] Y. Zhang, J. Železný, Y. Sun, J. Van Den Brink, and B. Yan, Spin Hall effect emerging from a noncollinear magnetic lattice without spin-orbit coupling, New Journal of Physics **20**, 073028 (2018).

[34] C.-T. Kuo, M. Neumann, K. Balamurugan, H. J. Park, S. Kang, H. W. Shiu, J. H. Kang, B. H. Hong, M. Han, T. W. Noh, and J.-G. Park, Exfoliation and Raman Spectroscopic Fingerprint of Few-Layer NiPS3 Van der Waals Crystals, Scientific Reports **6**, 20904 (2016).

[35] M. Bernasconi, G. L. Marra, G. Benedek, L. Miglio, M. Jouanne, C. Julien, M. Scagliotti, and M. Balkanski, Lattice dynamics of layered MPX3 (M=Mn,Fe,Ni,Zn; X=S,Se) compounds, Physical Review B **38**, 12089 (1988).

[36] K. Kim, S. Y. Lim, J.-U. Lee, S. Lee, T. Y. Kim, K. Park, G. S. Jeon, C.-H. Park, J.-G. Park, and H. Cheong, Suppression of magnetic ordering in XXZ-type antiferromagnetic monolayer NiPS3, Nature Communications **10**, 345 (2019).

[37] H. Matsuyama, C. Haginoya, and K. Koike, Microscopic Imaging of Fe Magnetic Domains Exchange Coupled with Those in a NiO(001) Surface, Physical Review Letters **85**, 646 (2000).

[38] U. H. Pi, K. W. Kim, J. Y. Bae, S. C. Lee, Y. J. Cho, K. S. Kim, and S. Seo, Tilting of the spin orientation induced by Rashba effect in ferromagnetic metal layer, Applied Physics Letters **97**, 10.1063/1.3502596 (2010).

[39] M. Hayashi, J. Kim, M. Yamanouchi, and H. Ohno, Quantitative characterization of the spin-orbit torque using harmonic Hall voltage measurements, Physical Review B **89**, 10.1103/PhysRevB.89.144425 (2014).

[40] A. Manchon, J. Železný, I. M. Miron, T. Jungwirth, J. Sinova, A. Thiaville, K. Garello, and P. Gambardella, Current-induced spin-orbit torques in ferromagnetic and antiferromagnetic systems, Reviews of Modern Physics **91**, 035004 (2019).

[41] C. O. Avci, *Current-induced effects in ferromagnetic heterostructures due to spin-orbit coupling*, Ph.D. thesis, ETH Zurich (2004).

[42] L. Neumann and M. Meinert, Influence of the Hall-bar geometry on harmonic Hall voltage measurements of spin-orbit torques, AIP Advances **8**, 10.1063/1.5037391 (2018).

[43] The SOT values for D1 were corrected by dividing the obtained values by a factor of 0.67 (for $W_2/W_1 = 0.83$) and for D2 by a factor of 0.72 (for $W_2/W_1 = 0.67$)[42].

[44] G. M. Stiehl, R. Li, V. Gupta, I. E. Baggari, S. Jiang, H. Xie, L. F. Kourkoutis, K. F. Mak, J. Shan, R. A. Buhrman, and D. C. Ralph, Layer-dependent spin-orbit torques generated by the centrosymmetric transition metal dichalcogenide β-MoTe2, Physical Review B **100**, 184402 (2019).

[45] M. H. Nguyen, D. C. Ralph, and R. A. Buhrman, Spin Torque Study of the Spin Hall Conductivity and Spin Diffusion Length in Platinum Thin Films with Varying Resistivity, Physical Review Letters **116**, 10.1103/PhysRevLett.116.126601 (2016).

arXiv:2005.01368v1 [cond-mat.mes-hall] 4 May 2020

Supplementary material for Large interfacial spin-orbit torques in layered antiferromagnetic insulator $NiPS_3$/ferromagnet bilayers

C. F. Schippers,[1,*] H. J. M. Swagten,[1] and M. H. D. Guimarães[1,2,†]

[1] *Department of Applied Physics, Eindhoven University of Technology, P.O. Box 513, 5600 MB, Eindhoven, the Netherlands*

[2] *Zernike Institute for Advanced Materials, University of Groningen, P.O. Box 221, 9747 AG, Groningen, the Netherlands*

(Dated: December 22, 2024)

S-I. DETERMINATION OF ANOMALOUS HALL RESISTANCE

In order to obtain precise values for the spin-orbit torques (SOTs) from the second-harmonic Hall measurements, the anomalous Hall resistance needs to be determined for the measured devices. For this a probing AC current is driven in the Hall bar and the generated transverse voltage is measured – specifically the first harmonic transverse voltage – while rotating the sample in an external magnetic field. In contrast to the measurement in the main text, the sample is rotated around on of its in-plane directions such that the magnetic field (from the perspective of the sample) is rotated through the out-of-plane direction; i.e., in terms of Eq. 1 of the main text, θ is varied while ϕ is kept constant.

In Fig. S1 a series of anomalous Hall measurements for different external magnetic fields is shown. While a simple sinusoidal measurement as a function of out-of-plane field-angle θ is expected from Eq. 1 of the main text, the measurements shows a more complex behaviour. We attribute this to a sufficiently strong in-plane shape anisotropy of the Py layer due to its small thickness (6 nm) with respect to the other dimensions.

To account for this and extract the anomalous Hall resistance R_{A} two additional steps are added to the data analysis procedure. First the measurement is fitted only for angles

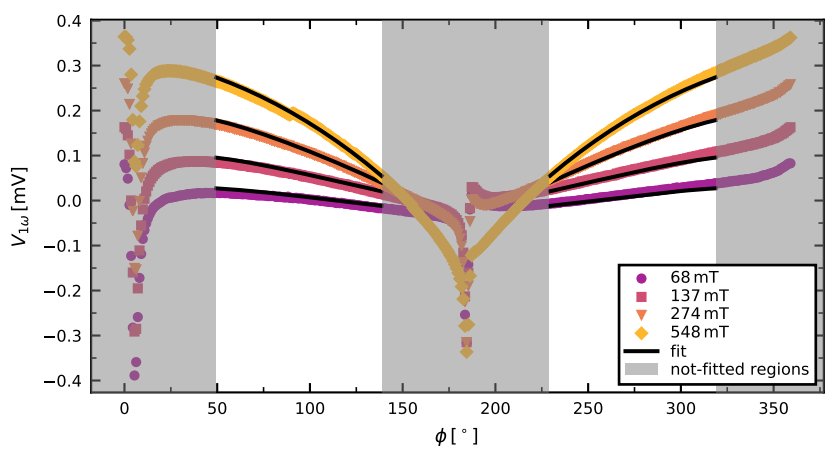

FIG. S1. Hall voltages of a Hall bar with $NiPS_3$/Py(6 nm) as a function of out-of-plane field-angle θ for varying magnetic field strengths at 300 K. The black lines are fits using Eq. 1 of the main text, with corrections for the misalignment of the magnetic field and magnetization due to demagnetization.

sufficiently far away from the out-of-plane direction (i.e. $|\theta| <= 45°$) as around the out-of-plane direction the measured Hall voltage is most influenced by the in-plane shape anisotropy. Further a simple energy model is used to correct for a discrepancy between the out-of-plane field-angle θ and the actual out-of-plane magnetization-angle θ_M; the model for calculating energy U is given by:

$$U = -\mathbf{B} \cdot \mathbf{M} + N_z \frac{1}{2} \mu_0 m_z^2 + N_x \frac{1}{2} \mu_0 m_x^2, \tag{S1}$$

where $\mathbf{B}$ and $\mathbf{M}$ are the external magnetic field and the Py magnetization, respectively, $m_{(x,z)}$ is x or z magnetization component, μ_0 is the magnetic permeability and N_z and N_x are the out-of-plane and in-plane demagnetization factor, respectively. As we are considering a thin magnetic film, we assume that $N_z \approx 1$ and that $N_x \ll 0.1$; i.e. an overall in-plane shape anisotropy with a small anisotropy within the plane. Moreover, we assume that the demagnetization is the dominant form of anisotropy in our system. Finally, also a possible exchange bias from the antiferromagnetic $NiPS_3$ is omitted since we experimentally found no evidence for an exchange bias within this system, as discussed later in Section S-V. In order to correct for the misalignment of the external magnetic field and the magnetization direction, a minimization routine for energy U has been incorporated into the fitting procedure, resulting in the fitted curves in Fig. S1.

Using these two corrections we are able to extract an anomalous Hall resistance from the AHE measurements.

A. Additional measurements of the anomalous Hall resistance

To show that the values for R_A are reasonable we measured the anomalous Hall resistance in a set-up where the magnetic field is swept between $\pm 2\,\mathrm{T}$, which suffices to saturate the Py layer. As using a device for this measurement rendered the sample useless for the second harmonic Hall measurements it is only performed on the Py/AlOx device for which measurements were shown in the main text.

In Fig. S2 the AHE measurement is shown for both current directions. The resistance was measured by driving an AC current of 1 mA (root-mean-square) at a frequency of 779 Hz and measuring the transverse voltage using a lock-in amplifier. A linear background and constant offset has been removed from the measurements to better determine R_A. In the measurement, we see that the resistance increases up to a field of $\pm 750\,\mathrm{mT}$, after which the

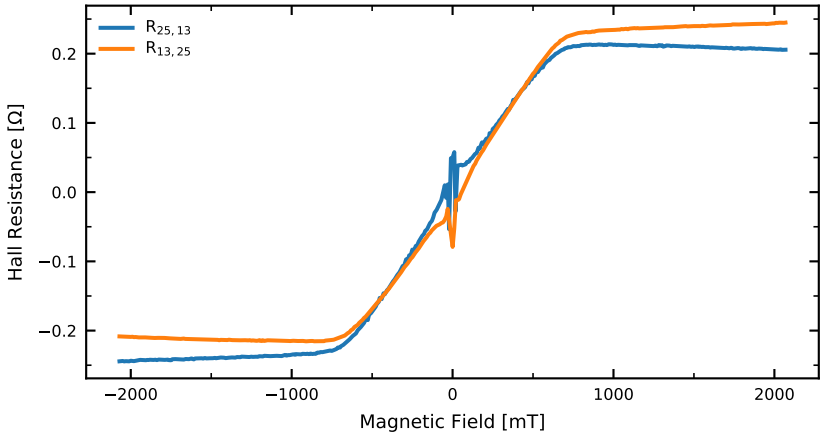

FIG. S2. Anomalous Hall resistance of a Hall bar with 6 nm of Py as a function of out-of-plane external magnetic field. A linear background has been removed from the measurements.

value saturates.

By averaging the (absolute value of) both high magnetic field directions we obtain $R_{\mathrm{A}} = (0.224 \pm 0.004)\,\Omega$ for the $R_{25,13}$ configuration and $R_{\mathrm{A}} = (0.226 \pm 0.001)\,\Omega$ for the $R_{13,25}$ configuration. Similar values (up to a factor of 2) were found in similar devices using the method described in the previous section. R_{A} is fairly similar for both current configurations, showing that we can safely use a single R_{A} value for correcting both current configurations of the second harmonic Hall measurement. This illustrates that the used R_{A} for interpreting the second harmonic Hall measurements should not affect the drawn conclusions.

S-II. EFFECT OF THE CURRENT DIRECTION ON THE SOTS

As a final check of the impact of the crystal symmetries on the spin-orbit torques, we repeated our measurements and analysis for interchanged current and Hall voltage directions. The results of these measurements are shown in different colours in Fig. S3a and b for out-of-plane field-like torque τ_{FL} and in-plane damping-like torque τ_{DL}, respectively. As the change in resistance of the devices and device geometry is taken into account during the measurements and subsequent analysis, we expect the obtained torques to be independent of the current direction if the crystal symmetry does not play a role in the measured torques[S2]. For the out-of-plane field-like torque τ_{FL} (Fig. S3a) this indeed is the case: the measured torques are virtually identical throughout the measured temperature range. However, for the

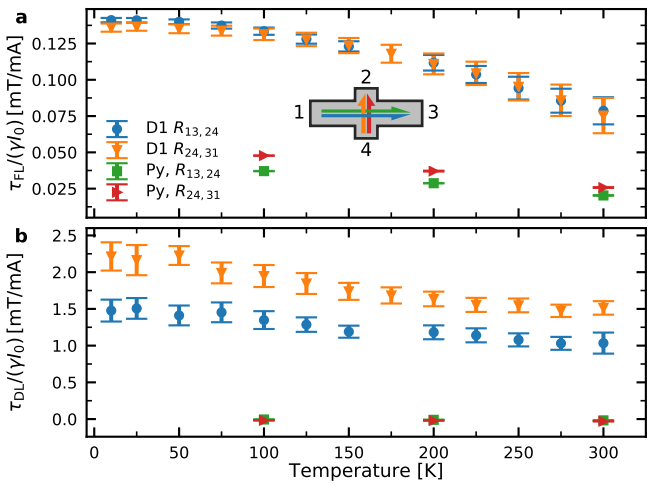

FIG. S3. Measured SOTs as a function of temperature temperatures for the out-of-plane field-like torque τ_{FL} (a) and the in-plane damping-like torque τ_{DL} (b) in the $NiPS_3$/Py device and a Py reference sample. The torques have been measured for two difference current directions as indicated in the sketch in (a); the voltage is always measured perpendicular to the applied current. $R_{ab,cd}$ indicates that the current is driven between contacts a and b and the Hall voltage is measured between contacts c and d. The torques have been corrected for the Hall bar geometry according to[S1].

in-plane damping-like torque τ_{DL} (Fig. S3b) a small difference occurs between the two current directions: τ_{DL} measured in one of the current directions is (throughout the temperature range) approximately 1.5 times larger than τ_{DL} measured in the other current direction. This behaviour is not exclusive to the torques measured in the $NiPS_3$/Py device; for the Py device this ratio between the torques measured for different current directions is approximately 2.3. Since this discrepancy occurs for both the $NiPS_3$/Py and Py devices, it suggests that it is related to a measurement artefact, most likely due to different current paths for the two configurations. Apart from this discrepancy, a very similar behaviour is found for τ_{DL}, independent of the current direction. This agrees with the conclusion drawn earlier that the torque is not related to the specific space group of the antiferromagnetic phase of $NiPS_3$.

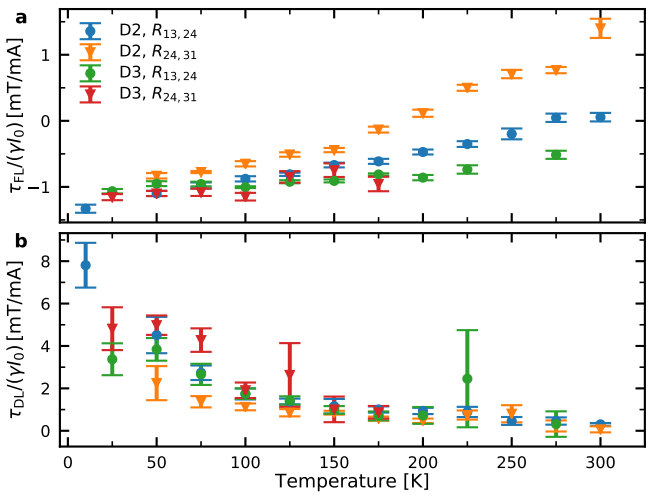

FIG. S4. Measurements of the out-of-plane field-like torque τ_{FL} (a) and the in-plane damping-like torque τ_{DL} (b) for two other $NiPS_3$/Py devices, named D2 and D3. The torques have been corrected for the Hall bar geometry according to[S1].

S-III. MEASUREMENTS OF ADDITIONAL $NIPS_3$/PY DEVICES

We performed similar measurements to the ones described in the main text for other $NiPS_3$/Py devices, named here devices D2 and D3. These devices were made on $NiPS_3$ crystals with different thicknesses from the device discussed in the main text, 6.34 nm and 5.15 nm for D2 and D3, respectively. Figure S4 shows the out-of-plane field-like torque τ_{FL} (a) and the in-plane damping-like torque τ_{DL} (b), for two current directions in these additional $NiPS_3$/Py devices.

We notice that the order of magnitude of the measured torques is consistent over the different devices, though the exact value differs from device to device. We observe that for most of our measurements, the out-of-plane field-like torque is negative, i.e. opposite to the torque expected from an Oersted-field coming from an unoxidised Al capping layer and increases in magnitude with a decrease in temperature. Interestingly, for device D2 with the current in one particular direction ($R_{24,13}$) we observe a positive out-of-plane field-like at room temperature with a sign change occurring at around 170 K. Since this behaviour is not reproduced for a different current configuration nor for other devices, we believe this is most likely due to some inhomogeneity in the current path.

For the in-plane damping-like torque, D2 and D3 show, similar to D1, an increase in

TABLE I. Measured torque values (both $\tau_{\mathrm{DL}}/(\gamma I_0)$ and $\tau_{\mathrm{FL}}/(\gamma I_0)$ in mT/mA) for the different $NiPS_3$/Py devices at room temperature (RT; 300 K) and at low temperature (LT; 50 K). Also the dimensions of the Hall bar (W_1 and W_2 in µm as defined in Fig. 1 of the main paper), the thickness of the $NiPS_3$ flake t_{NPS} (in nm), and the sheet resistance $R_{\mathrm{S}}^{\mathrm{RT}}$ (in $\Omega/\square$) at room temperature are given. The torques have been corrected for the Hall bar geometry according to[S1].

Device	W_1	W_2	t_{NPS}	$R_{\mathrm{S}}^{\mathrm{RT}}$	${\tau_{\mathrm{FL}}}^{\mathrm{RT}}/(\gamma I_0)$	${\tau_{\mathrm{FL}}}^{\mathrm{LT}}/(\gamma I_0)$	${\tau_{\mathrm{DL}}}^{\mathrm{RT}}/(\gamma I_0)$	${\tau_{\mathrm{DL}}}^{\mathrm{LT}}/(\gamma I_0)$
D1	3.0	2.5	3.1	140.7	0.079 ± 0.009	0.140 ± 0.002	1.0 ± 0.1	1.4 ± 0.1
D2	3.0	2.0	6.3	151.8	0.06 ± 0.06	-1.10 ± 0.04	0.30 ± 0.06	4.5 ± 0.9
D3	3.0	2.0	5.2	144.3	-	-0.95 ± 0.04	-	3.8 ± 0.5
Pt/Py	5.0	3.0	-	15.1	0.231 ± 0.001	0.2540 ± 0.0007	0.22 ± 0.01	0.23 ± 0.03
Py	5.0	3.0	-	112.0	0.0203 ± 0.0002	-	-0.018 ± 0.002	-

TABLE II. The torque conductivities σ_{FL} and σ_{DL} [in $10^4(\frac{\hbar}{2\mathrm{e}})/(\Omega\mathrm{m})$] is given at both room temperature (RT, 300 K and low temperature (LT, 50 K), assuming a saturation magnetization of $\mu_0 M_{\mathrm{S}} = 0.3\,\mathrm{T}$. Also the number of layers of the $NiPS_3$ flake ${n_{\mathrm{NPS}}}^{\mathrm{S3}}$, and the sheet resistance $R_{\mathrm{S}}^{\mathrm{RT}}$ (in $\Omega/\square$) at room temperature are given.

Device	n_{NPS}	$R_{\mathrm{S}}^{\mathrm{RT}}$	${\sigma_{\mathrm{FL}}}^{\mathrm{RT}}$	${\sigma_{\mathrm{FL}}}^{\mathrm{LT}}$	${\sigma_{\mathrm{DL}}}^{\mathrm{RT}}$	${\sigma_{\mathrm{DL}}}^{\mathrm{LT}}$
D1	4	140.7	0.73 ± 0.09	1.37 ± 0.02	10 ± 1	14 ± 1
D2	9	151.8	0.5 ± 0.6	-10.0 ± 0.4	2.6 ± 0.5	41 ± 8
D3	7	144.3	-	-8.6 ± 0.3	-	35 ± 5
Pt/Py	-	15.1	33.2 ± 0.1	38.5 ± 0.1	31 ± 1	35 ± 5
Py	-	112.0	0.395 ± 0.004	-	-0.34 ± 0.04	-

torque magnitude with a decrease in temperature, for all current directions. However, for devices D2 and D3 the increase in torque magnitude is steeper than found for device D1. For example in device D2 the torque reaches a value of $(8 \pm 1)\,\mathrm{mT/mA}$ at 10 K, an eightfold increase compared to the torque at room temperature. The measured torques and device parameters are summarized in Table I with device D1 being the one for which the data has been used for the main text. Table II summarizes the torque conductivities of the measured devices.

S-IV. TEMPERATURE DEPENDENCE OF THE ANOMALOUS HALL AND PLANAR HALL RESISTANCES

As a confirmation of the temperature dependence of the measured torques in the main text, the temperature dependence of both the planar Hall resistance R_{P} and the anomalous Hall resistance R_{A} were investigated. In Fig. S5 these temperature dependencies are shown. We observe a variation of both R_{P} and R_{A} as a function of temperature, which is also taken into account in our analysis for the extraction of the SOTs.

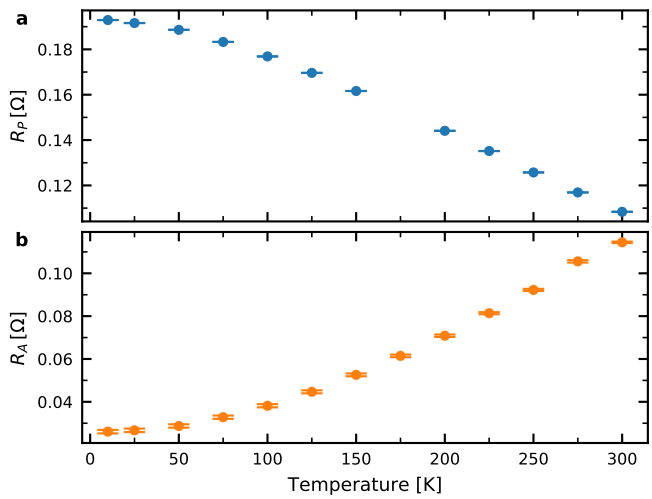

FIG. S5. Planar Hall resistance R_{P} (a) and anomalous Hall resistance R_{A} (b) as a function of temperature. For each temperature, the Hall resistances are determined from the average of the measured Hall resistances at that temperature.

S-V. ANISOTROPY AND EXCHANGE BIAS IN $NiPS_3$/PY DEVICES

During the analysis of both the first and second harmonic Hall measurements, we assumed a lack of in-plane anisotropy or exchange bias in our devices. Here we investigate if these assumptions are indeed valid. Fig. S6a shows the first harmonic Hall voltage $V_{1\omega}$ of the $NiPS_3$/Py device D1, discussed in the main text, along with a fit of Eq. 1 of the main text and the residue of the fit. Using this equation to fit the first harmonic Hall voltage implicitly assumes the absence of anisotropy; an additional anisotropy term is expected to cause a periodic addition to the first harmonic Hall voltage and would therefore show up in the residue of the fit. We indeed find a small periodic component in the fit residue, indicating

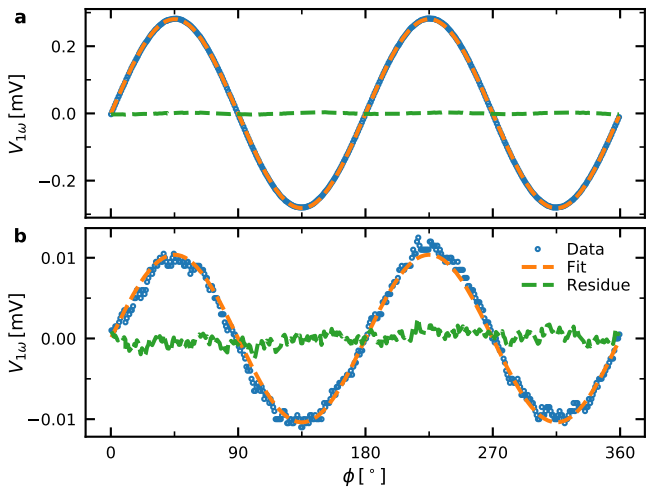

FIG. S6. Fit and residue of fit of the first harmonic Hall voltage in a $NiPS_3$/Py device. This is the same data as shown in Fig. 1 of the main text. For clarity purposes the residue of the fit is enlarged by a factor 10.

a very small anisotropy. However, as this periodic component is approximately 2 orders of magnitude smaller than the total first harmonic Hall voltage, we can safely assume that this anisotropy is sufficiently small to be disregarded in further analysis.

Similarly, we investigate if the absence of exchange bias in the Py layer due to the antiferromagnetic $NiPS_3$. Figure S6b shows the first harmonic Hall voltage of the $NiPS_3$/Py device after field-cooling the sample to 25 K in a magnetic field of 550 mT. In the residue of the fit using Eq.1 of the main text to the data, again a small periodic component can be found, indicating the possible presence of a small exchange bias due to the $NiPS_3$ layer. However, the periodic component is small compared to both the noise on the residue and the full amplitude of the first harmonic Hall voltage. Moreover, inducing this exchange bias requires field-cooling the devices, while for the actual measurements in the main text the samples were cooled without applying a magnetic field. Therefore, we can safely assume no exchange bias for the analysis of the measurements.

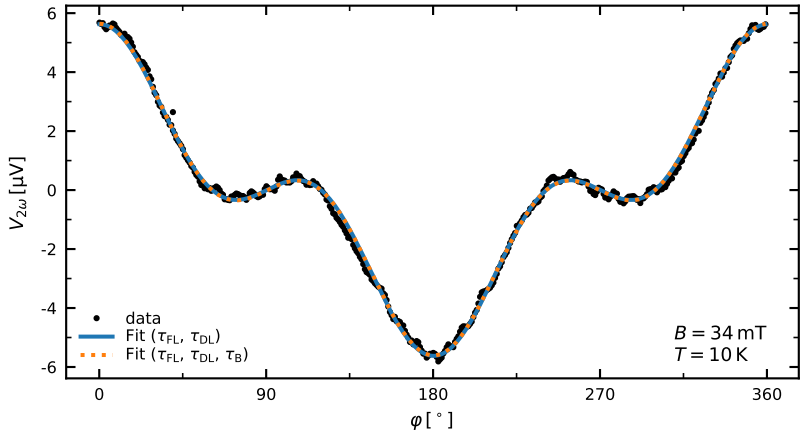

FIG. S7. Second-harmonic Hall measurement, taken at $T = 10\,\mathrm{K}$ and $B = 34\,\mathrm{mT}$, on device D1. The lines are two fits, excluding (blue solid line) and including (orange dashed line) contributions from the out-of-plane damping-like torque τ_B.

S-VI. FITTING AN OUT-OF-PLANE DAMPING-LIKE TORQUE

In order to investigate the presence of another type of SOT, the out-of-plane damping-like torque (τ_B) we have a closer look at fitting the second harmonic Hall measurement in Fig. S7. This measurement is taken at low temperature (10 K) and low field (34 mT) as the contribution of the in-plane damping-like torque is expected to be strongest. For investigating the presence of this torque we compare two fits to the second harmonic Hall voltage $V_\mathrm{H}^{2\omega}$ with a modified version of Eq. 2 of the main text[S4]:

$$V_\mathrm{H}^{2\omega} = -I_0(R_\mathrm{FL}\sin\varphi + R_\mathrm{B})\cos 2\varphi - \frac{1}{2}I_0 R_\mathrm{DL}\sin\varphi, \tag{S2}$$

where I_0 is the applied current, φ the angle of current with the magnetic field direction, and R_FL, R_DL, and R_B is the coefficient (with units Ω) proportional to τ_FL, τ_DL and the out-of-plane damping-like torque τ_B, respectively. By comparing a fit where R_B is fixed to zero with a fit where R_B is varied, we can determine if the R_B has a significant contribution and hence if τ_B is present.

Both of these fits are shown in Fig. S7. It is clear that adding R_B does not have a significant impact on the line-shape of the fit; the fits overlap both with each other and with the data. The values resulting of the fits also suggest that R_B does not have a significant influence. When varied, R_B is found to be $(6 \pm 4) \times 10^{-6}\,\Omega$, compared to $(1.42 \pm 0.01) \times 10^{-3}\,\Omega$

and $(1.369 \pm 0.008) \times 10^{-3}\,\Omega$ for R_{FL} and R_{DL}, respectively. Moreover, the values of both R_{FL} and R_{DL} do not vary (up to $1 \times 10^{-3}\,\%$, well within the margin of error) when R_{B} is fixed to zero instead of varied. Hence, we conclude that τ_{B} is not present in these devices.

---

* c.f.schippers@tue.nl

† m.h.guimaraes@rug.nl

[S1] L. Neumann and M. Meinert, Influence of the Hall-bar geometry on harmonic Hall voltage measurements of spin-orbit torques, AIP Advances **8**, 10.1063/1.5037391 (2018).

[S2] D. MacNeill, G. M. Stiehl, M. H. Guimarães, R. A. Buhrman, J. Park, and D. C. Ralph, Control of spin-orbit torques through crystal symmetry in WTe2/ferromagnet bilayers, Nature Physics **13**, 300 (2017).

[S3] C.-T. Kuo, M. Neumann, K. Balamurugan, H. J. Park, S. Kang, H. W. Shiu, J. H. Kang, B. H. Hong, M. Han, T. W. Noh, and J.-G. Park, Exfoliation and Raman Spectroscopic Fingerprint of Few-Layer NiPS3 Van der Waals Crystals, Scientific Reports **6**, 20904 (2016).

[S4] D. MacNeill, G. M. Stiehl, M. H. Guimarães, N. D. Reynolds, R. A. Buhrman, and D. C. Ralph, Thickness dependence of spin-orbit torques generated by WTe2, Physical Review B **96**, 054450 (2017).